Beilstein-Institut

1 nm Thick Functional Carbon Nanomembrane (CNM): New Opportunities for Nanotechnology

Min Ai and Armin Gölzhäuser*

Physics of Supramolecular Systems and Surfaces, University of Bielefeld, Universitätsstraße 25, 33615 Bielefeld, Germany

E-Mail: *ag@uni-bielefeld.de

Abstract

One nanometer thick, mechanically stable carbon nanomembranes (CNMs) are made by electron induced cross-linking of surface bound self-assembled monolayers (SAMs). The cross-linked SAMs are then released from the surface and can be placed onto solid materials or spanned over holes as free-standing membranes. Annealing at ~1000K transforms CNMs into graphene or graphenoids accompanied by a continuous change of mechanical stiffness and electrical resistance from insulating to conducting, which allows the tailoring of the CNM's electrical and mechanical properties. Recently, Janus membranes, i.e. CNMs functionalized by coupling different molecules to their top and bottom surfaces were built. Janus membranes have been built with functional polymers, proteins, and dyes, which demonstrates that Janus CNMs can act as platforms for two-dimensional chemistry. By combining different types of CNMs, hybrid nanolayers and biomimetic membranes can be built.

Introduction

Thin films are broadly and successfully integrated in many commercial products. They are used for surface lubrication, corrosion inhibition, or to avoid bio-fouling; other applications include barrier and separation membranes, light-emitting diodes, photo detectors, transistors, memory, and bio (chemical) sensors [1]. Most of these applications require a high thermal

and mechanical stability while it is desirable that the films are as thin as possible. Commercially available thin films have thicknesses ranging from a few 100 nm to several μm. However, due to their extremely large surface-to-volume ratio, we expect that films with a much smaller thickness (< 100 nm) would be even more attractive for fundamental studies as well as for industry. Several ways to fabricate ultrathin films are currently explored: layer-by-layer (LbL) films of polyelectrolytes [2], spin-coating [3], interfacial polymeric membranes [4], Langmuir-Blodgett [5], chemical vapor deposition, as well as the exfoliation of bulk materials into graphene [6, 7] or transition metal dichalcogenides [8].

Other fabrication strategies are based on molecular self-assembly. Self-assembled monolayers (SAMs) of amphiphilic molecules have the thickness of a single molecule, ~1 nm. When aromatic SAMs are exposed to radiation, they form cross-links between neighboring molecules. The resulting molecular network can be released from the surface as a free-standing two-dimensional carbon nanomembrane (CNM). As amphiphilic molecules have two distinct functional groups, the resulting CNM also has two sides of distinct chemical functionality, and both sides can be chemically modified with dissimilar molecules, resulting in "Janus membranes". CNMs can also be converted into graphene by annealing in ultra-high vacuum. This diverse chemistry and broad functionality open new pathways for fundamental and applied research.

This article summarizes recent progress in the fabrication, characterization and application of CNMs. The main text is organized into two sections, the first emphasizing on the synthesis and preparation strategies that have been developed for achieving the 1 nm thick CNMs, and the analysis techniques that were used to characterize their physical and chemical properties. The second part is to discuss prospects of their applications in nanotechnology, e. g. being potentially integrated in lab-on-a-chip technology, electronics and micro-/nano-electro mechanical systems.

FABRICATION AND CHARACTERIZATION OF CNMs

1. Fabrication

The first step in the making of CNMs is the preparation of a well-defined self-assembled monolayer of aromatic amphiphilic molecules on a surface. A SAM can be obtained by adsorption from solution or by vapor phase deposition in vacuum. Depending on types of molecules and surfaces, SAMs with different degrees of order form. These SAMs are then irradiated by electrons [9] or UV-light [10], which starts a dehydrogenation and recombination mechanism that leads to a two-dimensional cross-linking of molecules into a CNM [11]. After cross-linking, CNM is detached from the original surface and exhibits a free-standing ultra-thin film with a thickness of the length of the SAM molecule (about 1 nm for a biphenyl molecule) [12]. Examples are presented in Table 1.

Table 1. CNM formation from molecules on appropriate substrates by electron beam and agents.

| SAM	Anchor moiety	Substrate	Removing agent
Biphenylthiol or Nitrobiphenylthiol	-S	Au	I_2
Biphenylthiol or Nitrobiphenylthiol	-S	Cu	Ammonium persulfate + water
Biphenylcarboxylic acid	-COOH	Ag_2O	Ammonia solution (aq)
Biphenylhydroxamic acid	-CO-NH-OH	Fe/Ti	Acid/E-beam
Biphenylsilane or Hydroxybiphenyl	-OH or $-SiR_3$	Si	HF or KOH
Biphenylcarbonxylic acid or Nitrobiphenylcarboxylic acid	-COOH	ITO	Acid

2. Characterizing 1-nm-thick CNMs

Several analytical techniques for characterizing CNMs have been exploited. Among them optical microscopy, scanning electron microscopy (SEM), atomic force microscopy (AFM), helium ion microscopy (HIM), and transmission electron microscopy (TEM) provided an opportunity to study the morphology, optical and mechanical properties of CNM [13]. To elucidate the structure and composition of CNMs, spectroscopic techniques, such as infrared reflection absorption spectroscopy (IRRAS), X-ray and UV photoelectron spectroscopy (XPS, UPS), and Raman spectroscopy were utilized [9].

2.1 Imaging CNM

A 1 nm thick CNM is transparent in visible light. However, when it is placed onto a ~300 nm SiO_2 layer on a Si substrate, it can be detected with the naked eye, cf. Fig. 1 [13]. In Fig 1B, ribbons of CNMs on SiO_2/Si appear dark and blue shifted with respect to the substrate color in optical micrographs and two or three layers stacked on each other yield a higher contrast and blue shift, because of interference contrast, which results from light passing through layered structures with different dielectric properties, here the CNMs and the supporting SiO_2 on Si. Since interference contrast results in a clearly visible color change of the areas covered by CNMs and other thin nanofilms, it becomes a simple way of imaging such thin films.

CNMs were also imaged by helium ion microscopy (HIM). After being transferred onto metal grids, they became free-standing suspended on the holey support. Fig. 1C displays a free-standing CNM that spans over ~40 μm wide openings in metal grids, where finer structures, wrinkles, and defects are visualized. Scanning electron microscopy (SEM) can also be utilized to image CNMs by transferring them onto a perforated (2 μm holes) carbon

foil and directly imaging them by SEM (Fig. 1C (right)). If the same sample is imaged by HIM, (Fig. 1C (left)), the helium ion image reveals a much higher contrast than the SEM image.
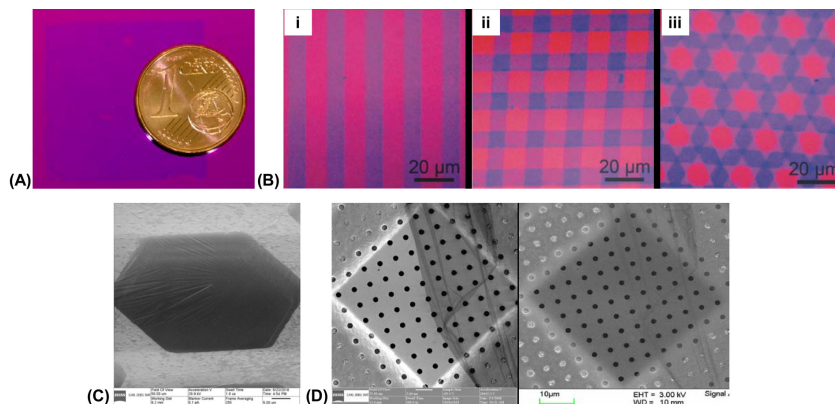
Figure 1. (A) Photograph of a cm^2-sized CNM (larger than one cent euro coin) on a SiO2/Si wafer. The CNM is visible due to Raleigh's interference contrast. (B) Optical micrograph of ~10 μm width CNM ribbons on a SiO2/Si wafer. i) A single layer. ii) Two layers transferred at a ~90° angle. iii) Three layers at an angle of ~60°. Each layer gives rise to a further blue shift. (C) HIM images of a CNM transferred onto a hexagonal pore (~40 μm in diameter). (D) Comparison of HIM and SEM images of a 1 nm thick CNM on a quantifoil TEM support.

## 2.2 Spectroscopic observation of the cross-linking

X-ray photoelectron spectroscopy was utilized to investigate the composition of SAMs, as well as radiation induced changes. Figure 2 displays C 1 s, N1 s, S 2 p, and O1 s spectra of 4-nitro-1,1'-biphenyl-4-thiol on a gold substrate, as recorded before and after irradiation by VUV under ultrahigh vacuum (UHV) conditions. The shift of the N1 s binding energy (BE) from 405.6 eV to 399.3 eV results from the chemical conversion of nitro groups to amino groups after irradiation with VUV. Characteristic changes also occur in the S 2 p and O1 s signals. A broadening of the S 2 p spectrum towards higher binding energies is attributed to a partial oxidation of the thiol species at the SAM/gold interface. The O1 s signal is significantly reduced after irradiation with VUV, which is explained by a loss of oxygen from nitro groups when they convert into amino groups. The thickness of SAM or CNM on the gold substrate can be determined from the attenuation of the Au4f$_{7/2}$ signal by the monolayer. The film thicknesses of SAMs (1.25 ± 0.8 nm) and CNMs (1.21 ± 0.9 nm) are obtained from these spectra [10].
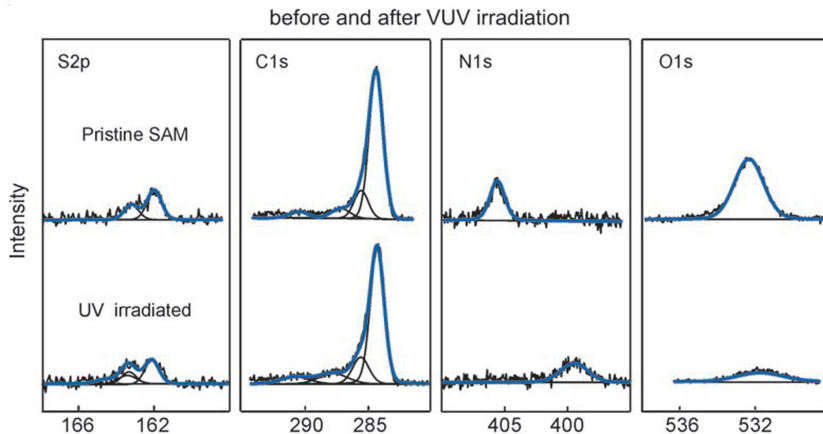
Figure 2. XP spectra of 4'-nitro-1,1'-biphenyl-4-thiol on gold before and after VUV (He I, 21.2 eV) irradiation. The generation of amino groups can be clearly recognized from the corresponding chemical shift from 405.5 eV to 399.2 eV [10].

2.3 Thermal stability

Thermal stability is important for the integration of CNMs in electronic devices. Turchanin, El-Desawy, and Gölzhäuser [14] found that cross-linked SAMs are thermally stable up to 1000 K. In their experiment, pristine SAMs and CNMs were heated on Au substrates in steps of $20-50$ K from room temperature to 1000 K, and then studied by XPS [14]. In Fig. 3A, after heating to 470 K, the C 1 s signal of the pristine SAMs showed only 10% of its initial intensity, indicating SAM decomposition or desorption, but the C 1 s signal of CNMs appears at 90% intensity. Figure 3B shows a plot of the intensity of the C 1 s signal of pristine and electron irradiated BPT as a function of temperature and dose. The pristine SAMs desorbed at about 400 K, and the XPS intensity of CNM after irradiation at 25 mC/cm^2 electron dosage lead to 50% loss. Upon annealing to 1000 K, 80% of the CNM XPS intensity was still observed after 45 mC/cm^2 electron dosage irradiation. Lower electron dosage leads to the partially cross-linked SAM.
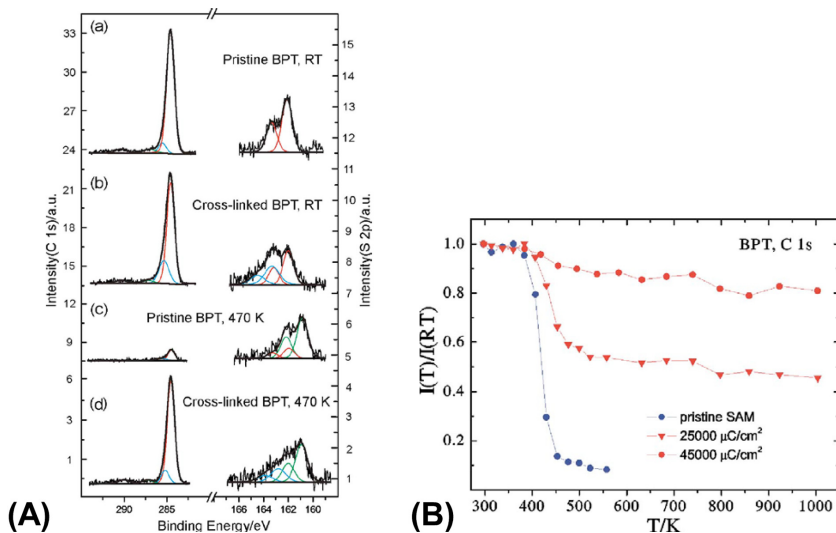
Figure 3. (A) XPS spectra of the C 1 s and S 2 p signals. (a) Pristine biphenythiol SAM (BPT) at room temperature. (b) Cross-linked BPT (45 mC/cm^2) at RT. (c) Pristine BPT after annealing at 470 K. (d) Cross-linked BPT after annealing at 470K. **(B)** Temperature dependence of the C 1 s signal of BPT as a function of irradiation dose [14].

## 2.4 Electrical resistance

The performance of CNMs in electronic devices, of course, depends on their electrical conductivity. The sheet resistance of CNMs that have been annealed at temperatures between 800 K and 1200 K was determined by a two-point measurement in UHV scanning tunneling microscopy (STM) and by four-point in ambient conditions. CNMs suspended on a gold grid were directly contacted by a STM tip in UHV. The resistance was determined from the current between the tip and the surrounding frame (Fig. 4A). CNMs were also transferred onto non-conductive silicon oxide and were then measured with four-probes (Fig. 4bB) [12]. Figure 4C shows the sheet resistivity as a function of the annealing temperature. After annealing CNMs at ~800 K, we find a sheet resistivity of ~10^{-8} kΩsq^{-1}, upon rising the annealing temperature to ~1200 K, this comes down to ~100 kΩsq^{-1}. The reason for this unusual behavior is that upon annealing CNMs transform into graphene and thus become conductive, as will be described in more detail in section 2.7.
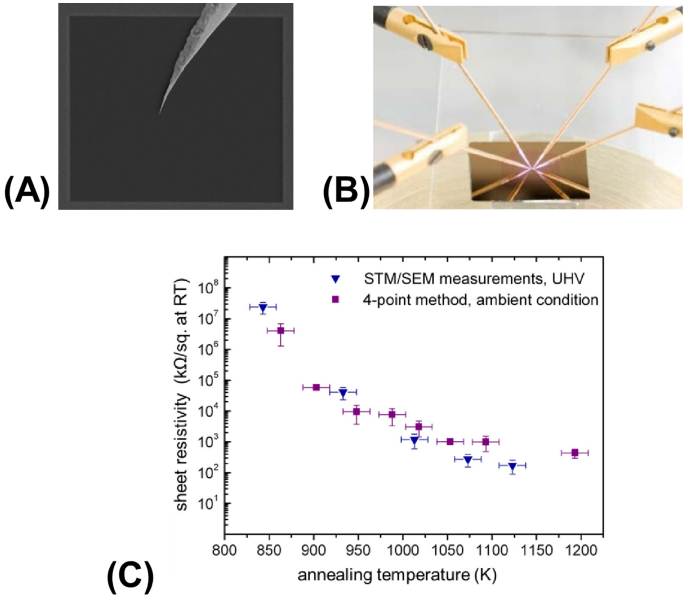
Figure 4. The resistivity of CNMs was determined by a two-point (STM) in UHV **(A)** and four-point in ambient conditions **(B)**. **(C)** The sheet resistivity corresponds to 10^{-8} kΩsq^{-1} after annealing at 800 K. Upon annealing to temperatures between 800 and 1200 K, the current/voltage curves are linear. Increasing the annealing temperature to 1200 K, the sheet resistivity drops to 100 kΩsq^{-1} [12].

Multilayers of CNMs after annealing show more conductivity than a single layer of CNMs, as in Fig. 5 [15]. Upon annealing to 1100 K, the sheet resistivity dropped further to 10.8, 30.3, and 37.2 kΩs q^{-1}, for five, four and three layers, respectively. This tunable electrical conductivity of CNMs from an insulator to a conductor by annealing temperatures or amounts of layers will be of value for CNMs to be utilized in micro- or nano-electronics.
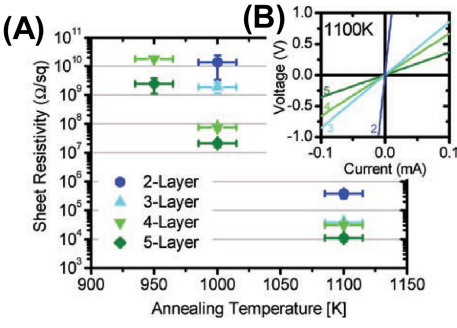
Figure 5. (A) RT sheet resistivity of BPT multilayers as a function of annealing temperature. The error bars represent the standard deviation of measurements at different spots on the samples. **(B)** RT linear current–voltage curves for 2-, 3-, 4-, and 5-layer samples after annealing at 1100 K [15].

2.5 Elastic properties

The elasticity of CNMs was investigated by Zhang, Beyer and Gölzhäuser [16] by using a bulge test method in an AFM for the determination of the Young's modulus and other quantities (Fig. 6). Gas pressure was applied to one side of a CNM that was freely suspended on a silicon substrate with a μm^2 opening. The pressure difference between the top and bottom side of the membrane resulted in a CNM deflection that was recorded by line-scanning the tip of an AFM (Fig. 6A) or by monitoring the deflection of a fixed AFM tip (central-point method, Fig. 6B). The central-point method has the advantage of reducing data acquisition time and lowering the probability that the CNM ruptures during the experiment. Young's modulus and internal stress have been calculated from the obtained pressure-deflection relationship. Maximum deflections several μm under at pressures up to 2 kPa were measured. The ultimate tensile strength reached $440-720$ MPa with elongation to break at values between $3-4\%$, and the Young's modulus was obtained in the range of 6 to12 GPa. The Young modulus depends on the precursors of CNMs or the electron doses for the cross-linking CNMs. Below 20 mC/cm^2, no free-standing CNMs were formed, whereas between 30 mC/cm^2 and 50 mC/cm^2, CNMs were formed. With further irradiation, the Young's moduli remained constant, even when the CNM was irradiated with much higher doses of up to 80 mC/cm^2. This result was in accordance with the thermal stability experiments of CNMs, which indicated almost complete cross-linking at an electron dose of ~45 mC/cm^2 [16].
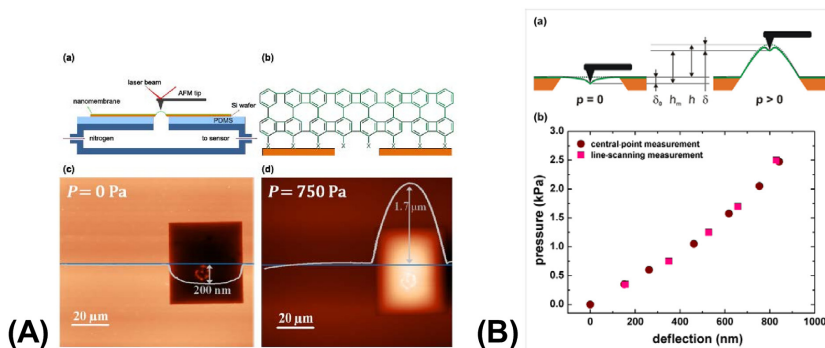

Figure 6. (A) (a) Schematic diagram of an AFM bulge test; (b) CNM suspended over an opening on Si substrate. (c) AFM image of a non-pressurized CNM and a line profile with a downward deformation of 200 nm; (d) CNM under pressure of 750 Pa with an upward 1.7 μm deflection. **(B)** (a) Schematic of the central-point method; (b) Comparison of the line-scanning and the central-point method [16].

2.6 Chemical modification of CNM surfaces

The chemical modification of CNMs primarily depends on the functionality of the precursor molecules. When CNMs made from 4'-nitro-1,1'-biphenyl-4-thiol molecules are electron irradiated, the hydrogen released during the cross-linking is reducing the terminal nitro groups to amino groups. These can be further functionalized with other molecules[17, 18], polymers [19 – 21] and proteins [22], as is shown in the schematic representation in Fig. 7.
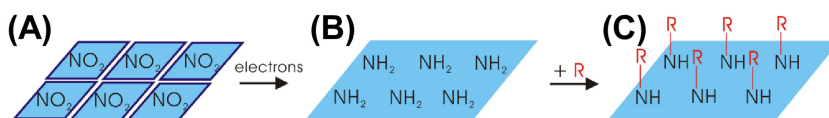

Figure 7. Scheme of electron induced chemical lithography: **(A)** 4'-nitro-1,1'-biphenyl-4-thiol monolayer. **(B)** An electron beam converts the terminal nitro groups of a 4'-nitro-1,1'-biphenyl-4-thiol monolayer to amino groups while the underlying aromatic layer is cross-linked. **(C)** The cross-linked amino biphenyl thiol region is used for the selective coupling of molecules R (small molecules, or proteins, or polymers).

An example are polymer brushes that can be grown onto CNMs by surface-initiated polymerization (SIP) [20, 21], or self-initiated surface photopolymerization and photografting (SIPGP) [22]. In Fig. 8, poly(4-vinyl pyridine) (P4VP) brushes were prepared on CNMs by SIPGP. In different solvents and depending on the pH values the morphology of the polymer brushes changes. In aqueous solution at pH = 7, the P4VP brushes are non-transparent on glass slides (Fig. 8B). This results from strong buckling due to collapsed polymer chains with low solubility. In ethanol or aqueous solutions at pH = 2.5, the P4VP brushes appear transparent on glass and flat on gold substrate (Fig. 8A and 8C), as ethanol is a very good solvent for P4VP and at low pH values the polymers tend to dissolve in aqueous solution due to the protonated pyridine group. This visible response of the CNM bound polymer brush to solvent stimulus may be useful for actuators, sensors, or displays, providing opportunities to adjust a surface to an environmental stimulus.
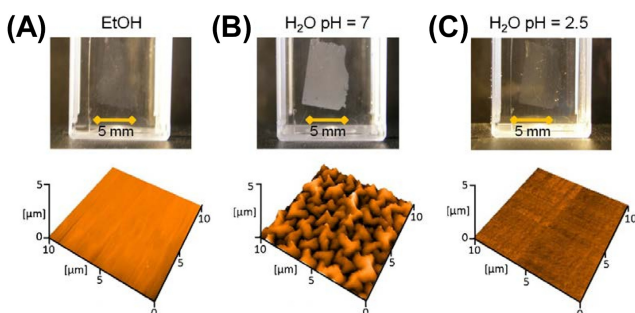

Figure 8. Photographs (above) and AFM measurements (below) of P4VP carpets in **(A)** ethanol, **(B)** water at pH 7, and **(C)** water at pH 2.5 [22].

CNMs can also be decorated with distinct functional groups on both sides. One side of the CNM is occupied with the amino groups as aforementioned, while the other bears sulfur residues after separation from Au. Both sides can react with other groups, and "Janus" CNMs that utilize this particularity have been constructed by Zheng *et al.* [24], who immobilized electron donors tetramethylrhodamine (TMR) to the top and electron acceptors (ATTO647N) to the bottom side of the same CNM. The synthesis processes are schematically displayed in Fig. 9. Figure 10 shows fluorescence micrographs and SEM images of CNMs functionalized on its amino side with TMR and on the thiol side with ATTO647N. The fluorescence resonance energy transfer (FRET) efficiency from the electron donor to the electron acceptor through the short spacer (~1 nm thick CNM) was determined to be effectively 100%, while the distance is much shorter than the Förster radius. This demonstration of "Janus" CNMs could lead to a platform for two-dimensional chemistry [24].
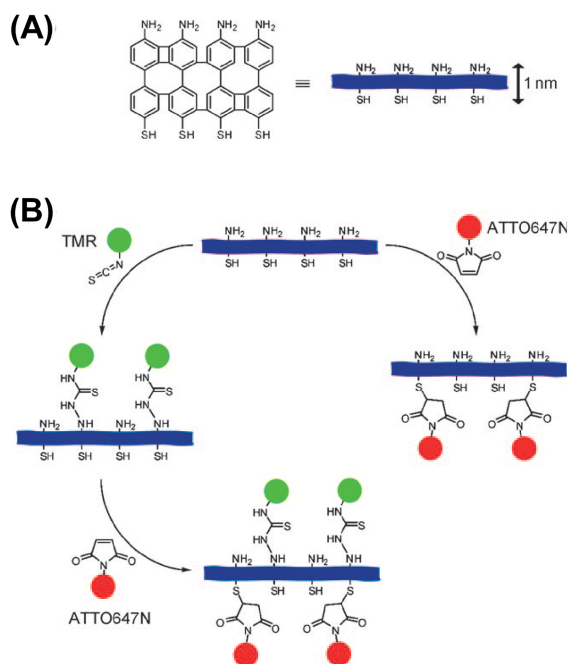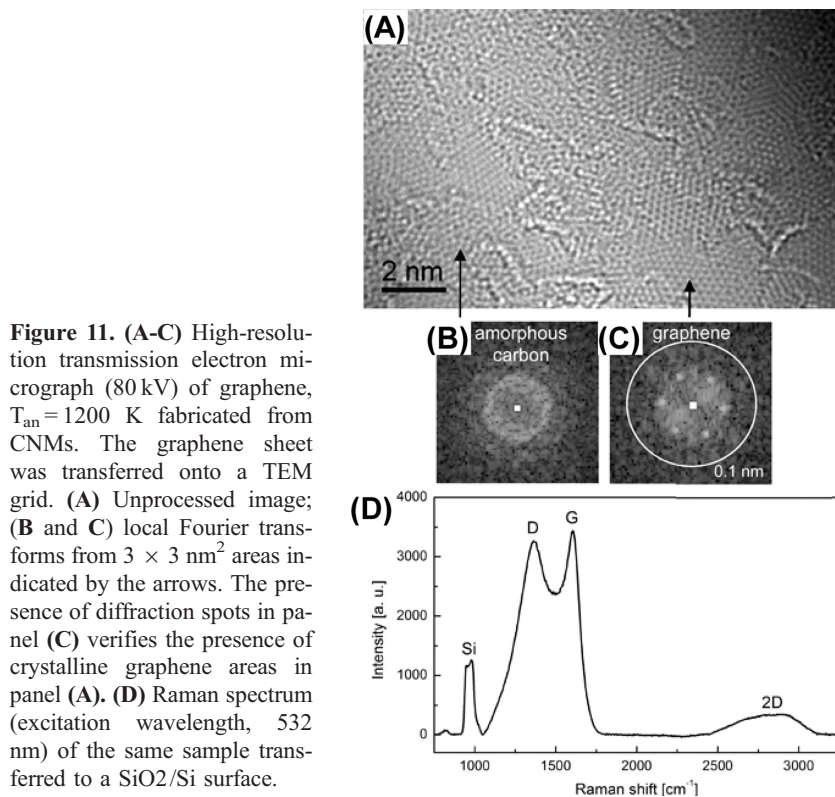
Figure 9. (A) A nanomembrane made from cross-linked biphenyl self-assembled monolayers. The 1 nm thick membrane has amino and thiol functional groups on its upper and lower sides, respectively. **(B)** Functionalization with fluorescent dyes of the upper and lower sides of the nanomembranes. The amino side is functionalized with TMR, the thiol side with ATTO647N.
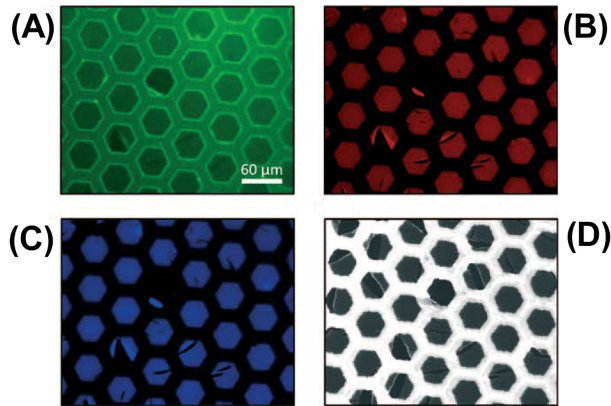
Figure 10. (A, B) Fluorescence and **(C)** FRET images, and **(D)** the corresponding SEM image of a nanomembrane functionalized on its upper and lower sides with TMR and ATTO647N, respectively. The FRET image has been recorded by exciting at the donor wavelength and recording the fluorescence emission in the acceptor channel. All micrographs show the same area of the nanomembrane [23].

2.7 Transforming CNMs into graphene

CNMs transform into graphene when they are heated in ultrahigh vacuum to temperatures up to 1200 K (pyrolysis). This has been demonstrated by Turchanin *et al.* [12, 15] by investigating the pyrolyzed CNM with the help of Raman spectroscopy, conductivity measurements (also see 2.4.), and transmission electron microscopy. The Raman spectrum of untreated CNMs does not show any peaks between 1000 and 2000 cm^{-1}. Upon annealing, the G-peak at 1605 cm^{-1}, that is characteristic for graphene, appears. Parallel, a rise of up to 5 orders of magnitude in the electrical conductivity is observed when the annealing temperature increases from room temperature to 1200 K, see figure 4. This is due to the formation of nanosized graphene crystallites in annealed CNMs. Furthermore, ordered domains comprised of individual atoms in annealed CNMs were observed by HRTEM (Fig. 11). Utilizing this bottom-up route from CNMs, graphene can be manufactured with well-defined thicknesses and tunable electrical properties on various metal and insulator substrates. This unique resistance behavior allows to tune CNMs from insulator to conductor.

Figure 11. (A-C) High-resolution transmission electron micrograph (80 kV) of graphene, $T_{an} = 1200$ K fabricated from CNMs. The graphene sheet was transferred onto a TEM grid. **(A)** Unprocessed image; (**B** and **C**) local Fourier transforms from 3×3 nm^2 areas indicated by the arrows. The presence of diffraction spots in panel **(C)** verifies the presence of crystalline graphene areas in panel **(A)**. **(D)** Raman spectrum (excitation wavelength, 532 nm) of the same sample transferred to a SiO2/Si surface.

OPPORTUNITIES FOR NANOTECHNOLOGY

Interest in CNMs is motivated by their unique properties, the tunable electrical conductivity, stiffness and surface chemistry. A variety of applications for CNMs have been proposed, and here we discuss CNMs as nanotemplates, nanopores and in biochips.

Nanotemplates are low dimensional substrates having artificially or naturally patterned structures. They can be created by non-covalent interactions, for example, hydrogen bonding, metal-organic coordination and charge transfer, van der Waals interactions [24]. The patterned structures can provide a controlled shape and composition; nanotemplates have attracted much interest in molecular engineering and recognition. Patterned SAMs can be simply fabricated by electron exposures [25]. Such patterns which contain irradiated and non-irradiated regions are useful templates for material deposition on the micro- and nanoscale.

Nanopores have the ability to interact with atoms, ions and molecules not only at the surfaces, but throughout the bulk. They are broadly found in nature, e.g. in zeolite minerals or biomembranes. In recent years artificial nanoporous materials were fabricated to be

utilized for catalysis, gas separation, water purification and biomolecular separation [26]. Two-dimensional nanoporous materials, i.e. sieves, have a perspective in bioseparation or proton-exchange in fuel cell when being integrated in microfluidic or membrane systems.

Biochips, as used in microfluidic or "lab-on-chip" devices, reduce laboratory procedures and enable portable detection of agents. In the past decades, cell biotechnology for cell culture and secretion [27], protein biochips [28], DNA biochips[29] have been a significant expansion in research. The key to the success of microfluidic-based biotechnology is to immobilize biomolecules onto surfaces with high density. For integration of 2D CNMs in biochips, the immobilization of biomaterials is indispensable. Biomolecules such as proteins and cells have been reported to be immobilized on the chemically tailored CNMs or physically adsorbed on CNMs [10, 30].

1. Micro- and nanotemplates

Micro- and nanotemplates can be used to fabricate metallic nanostructures on electrodes. An electrochemical surface template can be generated with structured SAMs. The SAMs are patterned by electron exposures through stencil masks with holes down to 1 μm and the subsequent electrodeposition of copper on SAM patterned gold electrodes has been demonstrated. In non-irradiated biphenyl SAMs, the copper peak in the cyclic voltammogram was observed at 0.08 V from the $CuSO_4/H_2SO_4$ electrolyte solution. For electron irradiated SAMs, the deposition peak was shifted to more negative potentials ($\Delta E = 0.15$ V). The electrodeposition of copper nanostructures was thus selectively generated on SAM templates at a deposition potential of +0.05V, where the irradiated biphenyl perfectly inhibited the copper deposition, as shown in Fig. 12 [31, 32].
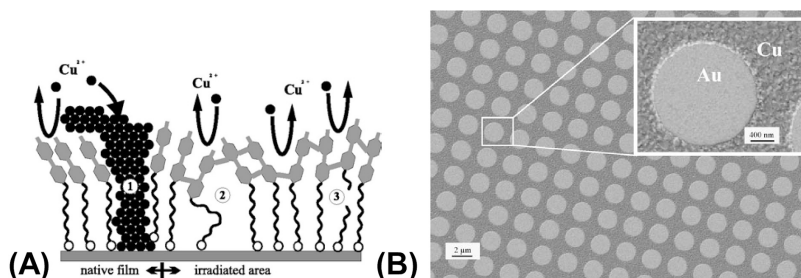

Figure 12. (A) Schematic illustration of the electrochemical behavior of a BP12 SAM. For the native film copper deposition is expected to be defect mediated (1). Electron irradiation links the biphenyl moieties which can then mask intrinsic defects (2) or radiation induced damage in the alkane spacer (3). **(B)** SEM-micrograph of Cu structures deposited on a BPT SAM template patterned by proximity printing (300 eV, 64000 μC/cm^2). Deposition parameters: 10 mM $CuSO_4$, +0.05 V (vs. NHE), 120 s [31, 32].

2. Micro- and nanopores

To drill holes in a 1-nm-thick film CNMs, fast and low-cost methods were demonstrated. Photolithography can be used to define the size and shape of pores that are then etched away by UV/ozone, cf. Fig. 13 [33]. In a more advanced method periodic nanopores are fabricated by extreme UV interference lithography (Fig. 14). The size of the nanopores can be flexibly tuned by choosing proper EUV masks, with a lower limit of currently ~20 nm [34].
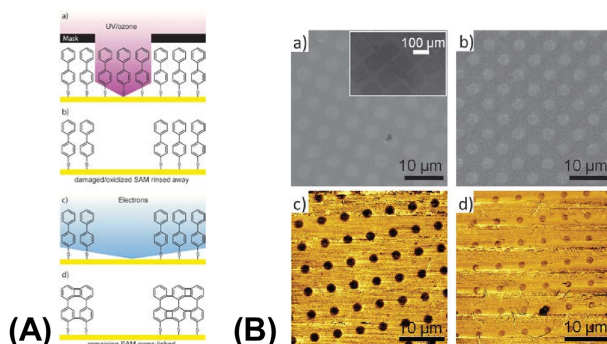
Figure 13. (A) (a) A SAM of BPT is exposed to UV/ozone through a mask. (b) The damaged/oxidized SAM in the exposed regions is rinsed away and (c) exposed to electrons. (d) The remaining SAM is cross-linked. **(B)** (a) SEM image of a BPT SAM after UV/ozone patterning through a TEM grid with 3 μm circular holes. (b) SEM after cross-linking (a) with an electron dose of 50 mC/cm^2. (c) LFM of a UV/ozone patterned BPT-SAM. (d) LFM of (c) after cross-linking [33].
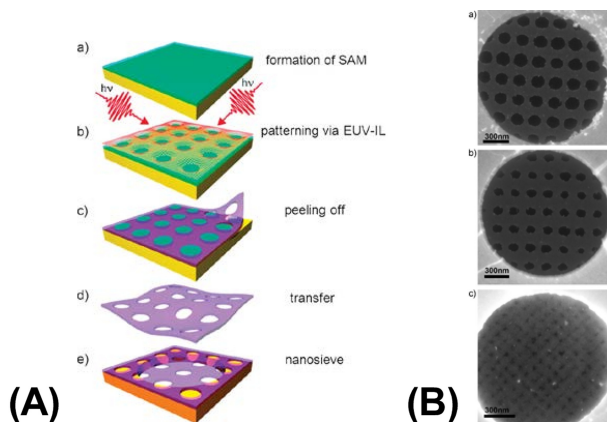
Figure 14. (A) Fabrication scheme of nanosieve membranes. (a) A SAM of NBPT is formed on a gold substrate. b) Generation of amino-terminated crosslinked areas (nanosheets) in the SAM via EUV-IL. c) Spin-coating of a polymer film and peeling off from the gold substrate. d) Transfer of the nanosheet with the hardened polymer. e) Formation of a 1-nm-thin freestanding nanosieve by dissolving the polymer on a new holey substrate.

(B) TEM characterization of nanosieve membranes. Dark-field mode images of ~1-nm-thin nanosieves with a) 138 ± 17-nm holes (interference grating periodicities of 225×200 nm^2; irradiation dose of 70 J cm^{-2}), b) 100 ± 15-nm holes (interference grating periodicities of 225×200 nm^2; irradiation dose of 120 J cm^{-2}), and c) 31 ± 6-nm holes (interference grating periodicities of 100×90 nm^2; irradiation dose of 50 J cm^{-2}) [34].

3. Biochips

3.1 Chemically tailored CNMs

To demonstrate CNMs as protein chips Turchanin, Tinazli and co-workers used the barrel-shaped 20S proteasome complex from the archaea Thermoplasma acidophilum as a biological model system periodically binding on CNMs [22]. The macromolecular proteins were engineered on CNMs via complexation between histidine-tagged proteins and transition metal ions, Ni (II). The Nickel-nitrotriacetic acid (NTA) and histidine-tagged chelator system is a powerful and universal tool for the one-step isolation and purification of gene products [35]. For the application in protein arrays and biosensors, long-term stability is required to overcome the limitation of metal leaching and rapid protein dissociation [36]. Therefore, the authors introduced cumulated NTA clusters on CNMs with multivalent interaction sites to load and regenerate His6-tags proteins. This concept of periodically binding proteins on CNMs shed light on immobilizing and then detecting single proteins as a biochip, as shown in Fig. 15.
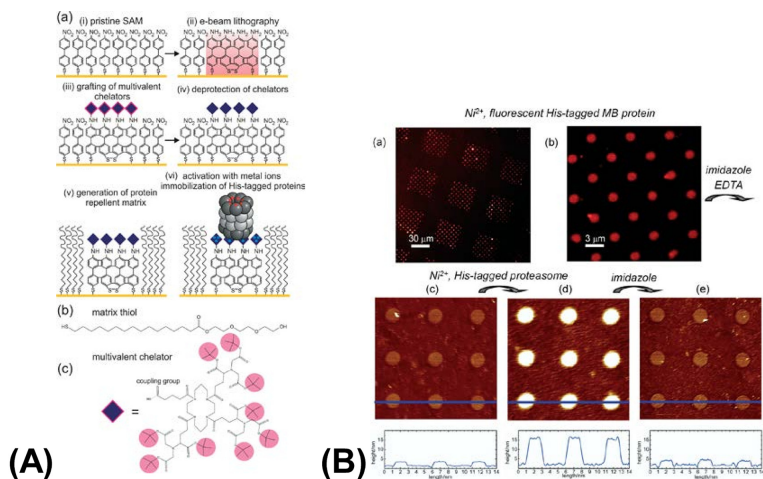
Figure 15. (A) Schematic representation of the protein chip assembly, (i–v); Controlled immobilization of His-tagged protein complexes (here: proteasome) in end-on orientation (vi). b) Protein repellent EG3-OH matrix thiols. c) Multivalent tris-NTA chelator with protected carboxyl functionality. (B) Controlled immobilization of different proteins on the chip surface. a, b) Confocal laser scanning microscopy images of specifically immobilized Atto565-labeled maltose-binding proteins (His10-MBP). c) Topographic AFM image of the same chip after the regeneration with imidazole. d) In situ AFM scan of a microarray of immobilized His6-proteasome complexes. e) The same surface after regeneration. AFM images are 14×14 µm^2, the z-scale corresponds to 20 nm [22].

3.2 Physically immobilized on CNMs

Non-covalent interaction (van der Waals and electrostatic forces) between biomolecules and CNMs provides an alternative and simple way to investigate the biocompatibility of CNMs. Rhinow *et al.* have prepared purple membranes (PMs) from *Halobacterium salinarum*, a 2-D crystalline monolayer of bacteriorhodopsin and lipids as a test specimen on CNMs [37]. Characterization of PM on CNMs by cryogenic high-resolution transmission electron microscopy (cryo-EM) (Fig. 16 B) reveals that trehalose embedded PM samples have been imaged on CNMs, and the amplitudes as well as phases can be recovered up to high resolution ranges. The biocompatibility of CNMs to PMs is further confirmed with tapping-mode AFM in a buffer solution. The 2D crystal lattice of PMs on CNMs was visualized, and the force spectroscopy obtained by AFM exhibited non-folding peaks, due to the extracellular side of PM's physical adsorption on CNMs [37].
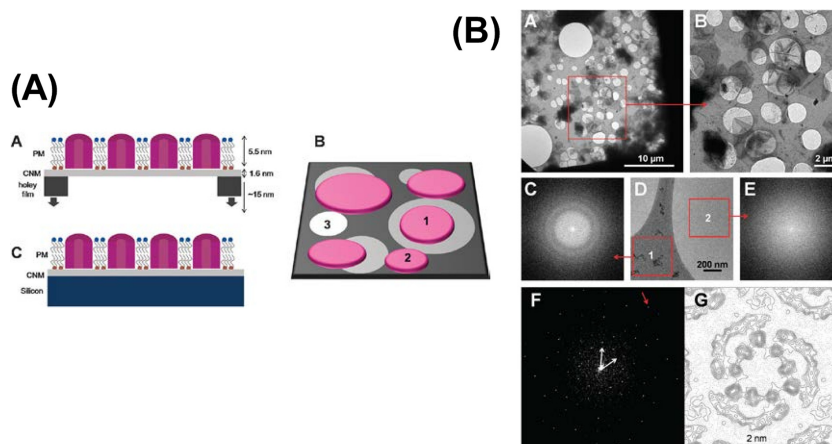
Figure 16. (A) Schematic representation of PMs on CNMs. (A) PMs on freestanding CNMs. PMs and CNMs are drawn on scale with respect to their thickness. (B) (1) PMs sticking to freestanding CNMs, (2) PMs supported by CNMs plus thick carbon support, and (3) holey carbon without CNMs. (C) PMs on silicon-supported CNMs.

(B) (A) TEM image of trehalose-embedded PMs on CNMs at room temperature. A holey carbon film supports the CNM. (B) Enlarged view of the central area of (A) (red square). (C) FFT of area 1 of (D). Thon rings are visible due to phase contrast of the thick holey carbon support. (D) TEM image of a sample-free CNM area, which spans two adjacent holes. (E) FFT of free-hanging CNM (area 2 of (D)). Thon rings are absent. (F) Fourier transform of an image of a single trehalose-embedded PM on cCNM at liquid nitrogen temperature. White arrows indicate the unit cell vectors corresponding to the 62.4 Å lattice. The red arrowhead points to the (4, 3) reflection at 8.9 Å resolution. (G) A projection map of PMs on CNMs at 4 Å resolution as calculated from eight averaged images in a defocus range of 500 – 1000 nm [37].

CONCLUSIONS AND OUTLOOK

This article provides an overview on recent trends in CNM research. The fabrication of CNMs from various self-assembled small aromatic molecules of a variety of substrates has been reviewed. The exploration of the properties of these two-dimensional films was revisited, among them the tuning of its chemical, mechanical and electronic function, and its conversion to graphene after pyrolysis. Janus CNM in which the top of the CNM is decorated with electron donors and while its bottom with electron acceptors, and their used as "rulers" to determine the length (generally 1 nm ~ 8 nm) of a molecular spacer between donor and acceptor incorporated by biomolecules is discussed. When both sides of the CNM are decorated with site-specific biomolecules, CNMs can be utilized to mimic biological membranes. There is a range of further applications in nanoscience and nanotechnology, for instance, micro- or nanotemplates, micro- or nanopores and biochips. The tunable conductivity and surface chemistry will permit CNMs to be integrated in lab-on-a-chip devices for liquid or gas separation, electronics, MEMS/NEMS devices in the near future. Opportunities and challenges co-exist, for example, in developing new routes for preparing CNMs of macroscopic size, and understanding the detailed nanostructures of CNMs. These unsolved fundamental questions together with potential applications will provide compelling motivation for CNM research in the coming years.

ACKNOWLEDGEMENTS

REFERENCES

[1]   Huang, G., Mei, Y. (2012) *Adv. Mater.* **24**:2517 – 2546.
        http://dx.doi.org/10.1002/adma. 201200574.

[2]   Decher, G., (1997**)** *Science* **277**:1232 – 1237.
        http://dx.doi.org/10.1126/science.277.5330.1232.

[3]   Vendamme, R., Onoue, S.-Y., Nakao, A., Kunitake, T. (2006) *Nature Materials*
        5:494 – 501.
        http://dx.doi.org/10.1038/nmat1655.

[4]   Louie, J. S., Pinnau, I., Reinhard, M. (2008) *J. Membr. Sci.* **325**:793 – 800.
        http://dx.doi.org/10.1016/j.memsci.2008.09.006.

[5]   Nardin, C., Winterhalter, M., Meier, W. (2000) *Langmuir* **16**:7708 – 7712.
        http://dx.doi.org/10.1021/la000204t.

[6]   Li, X., Cai, W., An, J. (2009) *Science* **324**:1312 – 1314.
        http://dx.doi.org/10.1126/science.1171245.

[7]   Novoselov, K. S., Geim, A. K., Morozov, S. V., Jiang, D., Zhang, Y., Dubonos, S. V.,
        Grigorieva, I. V., Firsov, A. A. (2004) *Science* **306**:666 – 669.
        http://dx.doi.org/10.1126/science.1102896.

[8]   Chhowalla, M., Shin, H. S., Eda, G., Li, L.-J., Loh, K. P., Zhang, H. (2013) *Nature
        Chemistry* **5**:263 – 275.
        http://dx.doi.org/10.1038/NCHEM. 1589.

[9]   Eck, W., Küller, A., Grunze, M., Völkel, B., Gölzhäuser, A. (2005) *Adv. Mater.*
        17:2583 – 2587.
        http://dx.doi.org/10.1002/adma.200500900.

[10]   Turchanin, A., Schnietz, M., El-Desawy, M., Solak, H. H., David, C., Gölzhäuser, A.
        (2007) *Small* **3**:2114 – 2119.
        http://dx.doi.org/10.1002/smll.200700516.

[11]   Turchanin, A., Käfer, D., El-Desawy, M., Wöll, Ch., Witte, G., Gölzhäuser, A. (2009)
        Langmuir **25**:7342 – 7352.
        http://dx.doi.org/10.1021/la803538z.

[12]   Turchanin, A., Beyer, A., Nottbohm, C. T., Zhang, X., Stosch, R., Sologubenko, A.,
        Mayer, J., Hinze, P., Weimann, T., Gölzhäuser, A. (2009) *Adv. Mater.* **21**:1233 –
        1237.
        http://dx.doi.org/10.1002/adma.200803078.

[13]   Gölzhäuser, A., Wöll, Ch. (2010) *ChemPhysChem.* **11**:3201 – 3213.
        http://dx.doi.org/10.1002/cphc.201000488.

[14]   Turchanin, A., El-Desawy, M., Gölzhäuser, A. (2007) *Appl. Phy. Lett.* **90**:053102.
        http://dx.doi.org/10.1063/1.2437091.

[15]   Nottbohm, C. T., Turchanin, A., Beyer, A., Stosch, R., Gölzhäuser, A. (2011) *Small*
        7:874 – 883.
        http://dx.doi.org/10.1002/smll.201001993.

[16]   Zhang, X., Beyer, A., Gölzhäuser, A. (2011) *Beilstein J. Nanotechnol.* **2**:826 – 833.
        http://dx.doi.org/10.3762/bjnano.292.

[17]   Gölzhäuser, A., Eck, W., Geyer, W., Stadler, V., Weimann, T., Hinze, P., Grunze, M.
        (2001) *Adv. Mater.* **13**:806 – 809.
        http://dx.doi.org/10.1002/1521-4095(200106)13:11%3C803::AID-ADMA806%3E3.0.CO;2-W.

[18]   Nottbohm, C. T., Sopher, R., Heilemann, M., Sauer, M., Gölzhäuser A. (2010) *J. Bio. Tec.* **149**:267 – 271.
       http://dx.doi.org/10.1016/j.jbiotec.201001018.

[19]   Schmelmer, U., Jordan, R., Geyer, W., Eck, W., Gölzhäuser, A., Grunze, M., Ulman, A. (2003) *Angew. Chem. Int. Ed.* **42**:559 – 563.
       http://dx.doi.org/10.1002/anie.200390161.

[20]   Schmelmer, U., Paul, A., Küller, A., Steenackers, M., Ulman, A., Grunze, M., Gölzhäuser, A., Jordan, R. (2007) *Small* **3**:459 – 465.
       http://dx.doi.org/10.1002/smll.200600528.

[21]   Amin, I., Steenackers, M., Zhang, N., Beyer, A., Zhang, X., Pirzer, T., Hugel, T., Jordan, R., Gölzhäuser, A. (2010) *Small* **6**:1623 – 1630.
       http://dx.doi.org/10.1002/smll.201000448.

[22]   Turchanin, A., Tinazli, A., El-Desawy, M., Großmann, H., Schnietz, M., Solak, H. H., Tampé, R., Gölzhäuser A. (2008) *Adv. Mater.* **20**:471 – 477.
       http://dx.doi.org/10.1002/adma.200702189.

[23]   Zheng, Z., Nottbohm, C. T., Turchanin, A., Muzik, H., Beyer, A., Heilemann, M., Sauer, M., Gölzhäuser A. (2010) *Angew. Chem. Int. Ed.* **49**:8493 – 8497.
       http://dx.doi.org/10.1002/anie.201004053.

[24]   Cicoira, F., Santato, C., Rosei, F. (2008) *Top Curr. Chem.* **285**:203 – 267.
       http://dx.doi.org/10.1007/128_2008_2">10.1007/128_2008_2.

[25]   Gölzhäuser, A., Geyer, W., Stadler, V., Eck, W., Grunze, M., Edinger, K., Weimann, T., Hinze, P. (2000) *J. Vac. Sci. Technol. B* **18**:3414 – 3418.
       http://dx.doi.org/10.1116/1.1319711.

[26]   Davis, M. E. (2002) *Nature* **417**:813 – 821.
       http://dx.doi.org/10.1038/nature00785.

[27]   Yang, M., Yao, J., Duan, Y. (2013) *Analyst* **138**:72 – 86.
       http://dx.doi.org/10.1039/c2an35744e.

[28]   Rusmini, F., Zhong, Z., Feijen, J. (2007) *Biomacromolecules* **8**:1775 – 1789.
       http://dx.doi.org/10.1021/bm061197b.

[29]   Dutse, S. W., Yusof, N. A. (2011) *Sensors* **11**:5754 – 5768.
       http://dx.doi.org/10.3390/s110605754.

[30]   Biebricher, A., Paul, A., Tinnefeld, P., Gölzhäuser, A., Sauer, M. (2004) *Journal of Biotechnology* **112**:97 – 107.
       http://dx.doi.org/10.1016/j.jbiotec.2004.03.019.

[31] Kaltenpoth, G., Völkel, B., Nottbohm, C.T., Gölzhäuser, A., Buck, M. (2002) *J. Vac. Sci. Techno. B* **20**:2734 – 2738.
      http://dx.doi.org/10.1116/1.1523026.

[32] Völkel, B., Kaltenpoth, G., Handrea, M., Sahre, M., Nottbohm, C. T., Küller, A., Paul, A., Kautek, W., Eck, W., Gölzhäuser, A. (2005) *Surface Science* **597**:32 – 41.
      http://dx.doi.org/10.1016/j.susc.2004.08.046.

[33] Nottbohm, C.T., Wiegmann, S., Beyer, A., Gölzhäuser A. (2010) *Phys. Chem. Chem. Phys.* **12**:4324 – 4328.
      http://dx.doi.org/10.1039/B923863H.

[34] Schnietz, M., Turchanin, A., Nottbohm, C. T., Beyer, A., Solak, H. H., Hinze, P. T., Weimann, Gölzhäuser A. (2009) *Small* **5**:2651 – 2655.
      http://dx.doi.org/10.1002/smll.200901283.

[35] Hochuli, E., Bannwarth, W., Döbeli, H., Gentz, R. & Stüber, D. (1988) *Bio-Techniques* **6**:1321 – 1325.
      http://dx.doi.org/10.1038/nbt1188-1321.

[36] Nieba, L., NiebaAxamnn, S. E., Persson, A., Hamalainen, M., Edebratt, F., Hansson, A., Lidholm, J., Magnusson, K., Karlsson, A. F., Pluckthun, A. (1997) *Anal. Biochem.* **252**:217 – 228.
      http://dx.doi.org/10.1006/abio.1997.2326.

[37] Rhinow, D., Vonck, J., Schranz, M., Beyer, A., Gölzhäuser, A., Hampp, N. (2010) *Phys. Chem. Chem. Phys.* **12**:4345 – 4350.
      http://dx.doi.org/10.1039/b923756a.